metals

MDPI

Article

Annealing-Induced High Ordering and Coercivity in Novel $L1_0$ CoPt-Based Nanocomposite Magnets

Alina Daniela Crisan, Florin Vasiliu, Ionel Mercioniu, Cristina Bartha, Monica Enculescu and Ovidiu Crisan *

National Institute for Materials Physics, 077125 Magurele, Romania; a_crisan2002@yahoo.com (A.D.C.); fvasiliu@infim.ro (F.V.); imercioniu@infim.ro (I.M.); cristina.bartha@infim.ro (C.B.); mdatcu@infim.ro (M.E.)
* Correspondence: ocrisan@infim.ro; Tel.: +40-21-2418141

Received: 16 May 2018; Accepted: 12 June 2018; Published: 19 June 2018

Abstract: A novel class of quaternary intermetallic alloys based on CoPt is investigated in view of their interesting magnetic properties induced by the presence of hard magnetic $L1_0$ phase. A $Co_{48}Pt_{28}Ag_6B_{18}$ alloy has been prepared by rapid solidification from the melt and subjected to various isothermal annealing procedures. The structure and magnetism of both as-cast and annealed samples as well as the phase evolution with temperature are investigated by means of thermal analysis, X-ray, and selected area electron diffraction, scanning and high-resolution electron microscopy, and magnetic measurements. The X-ray diffraction (XRD) analysis shows that both the as-cast alloy and the sample annealed at 400 °C (673 K) have a nanocrystalline structure where fcc CoPt phase predominates. Annealing at 473 °C promotes the formation of $L1_0$ phase triggered by the disorder-order phase transformation as documented in the differential scanning calorimetry results. The sample annealed at 670 °C (943 K) shows full formation of $L1_0$ CoPt as revealed by XRD. Magnetic measurements showed coercivity values ten times increased compared to the as-cast state. This confirms the full formation of $L1_0$ CoPt in the annealed samples. Moreover, detailed atomic resolution HREM images and SAED patterns show the occurrence of the rarely seen (003) superlattice peaks, which translated into a high ordering of the $L1_0$ CoPt superlattice. Such results spur more interest in finding novel classes of nanocomposite magnets based on $L1_0$ phase.

Keywords: $L1_0$ phase; CoPt nanocomposite magnet; high-resolution electron microscopy; phase evolution; melt spun ribbons

1. Introduction

There has been a recent surge of interest in $L1_0$ CoPt-based alloys, mainly due to the hard magnetic properties of the tetragonal $L1_0$ phase: high magnetocrystalline anisotropy (10 MJ/m^3), high coercivity, high Curie temperature (450 °C) and high chemical stability combined with the lower temperature of $L1_0$-phase formation compared to the case of FePt $L1_0$ phase. These alloys were recently suggested as alternatives to the rare-earth permanent magnets and as potential candidates for patterned media in heat-assisted or microwave-assisted magnetic recording [1–5]. The ordered $L1_0$ materials such as FePt and CoPt feature magnetization stability against thermal fluctuations due to their high magnetocrystalline anisotropy. However, there are many challenges involved in obtaining the desired microstructure to achieve these good magnetic properties.

It is worth noting that the equilibrium phase of the stoichiometric CoPt bulk alloys at room temperature is the face-centered cubic disorder A1 phase. Only after appropriate annealing can the fcc phase be transformed into the face-centered tetragonal ordered $L1_0$ phase, which is magnetically hard.

The disorder-order transformation and its effect on remanence and coercivity enhancement in bulk, isotropic CoPt magnets has been studied by Xiao et al. [6]. They found that only after annealing

at 675 °C (948 K) does the disorder-order phase transformation take place in CoPt and the strong remanence enhancement effect is due to the multiple phase character of the samples, as it originates from exchange coupling between the face-centered-tetragonal (fct)-ordered hard magnetic phase and the face-centered-cubic (fcc)-disordered soft magnetic matrix.

The high ordering temperature is regarded as an obstacle for future utilization of such alloys as the next class of nanocomposite magnets. However, a reduction of the ordering temperature required for $L1_0$ phase formation can be obtained via suitable modulation of the stoichiometry, for example by adding other elements to the composition. In the case of the FePt system, noble metals such as Au, Ag or Nb have been considered as suitable additions, having the role of promoting early ordering by segregation to the (Fe,Co)Pt grain boundaries [7–14] while a glass-forming element such as boron has been added to FePt to allow synthesis by out-of-equilibrium techniques such as rapid solidification from the melt [15–21].

Chang et al. [22] have studied the effect of Co substitution on the magnetic properties of melt-spun (Fe,Co)-Pt-B nanocomposite ribbons and found that Co substitution enhances the coercivity and energy product due to the formation of ordered $L1_0$-(Fe,Co)Pt phase with higher anisotropy field. Makino et al. [23] obtained the crystalline ordered $L1_0$-FePt phase, with high coercivity, directly formed by rapid quenching of the melt in (Fe,Co)-Pt-Zr-B system, in the compositional range of 2–5 at. % Zr and 17–20 at. % B, without passing through an amorphous precursor. Conversely, Inoue and Zhang [24] obtained a multiphase nanocomposite (Fe,Co)-Pt-B with good permanent magnet properties only after annealing of the amorphous precursor obtained by rapid solidification from the melt. The main difference with respect to the formation or not of an amorphous precursor is the amount of B. While Makino et al. [23] has 17–20 at. % in their initial composition, Inoue and Zhang [24] had 25 at. % B in their initial composition, therefore they obtained an initially amorphous as-cast state and the $L1_0$ phase has been obtained only after subsequent annealing. The good hard magnetic properties are considered to be due to exchange magnetic coupling between nanoscale hard face-centered-tetragonal and soft face-centered-cubic magnetic phases [24].

In Co-rich alloys with low Pt concentration, Yoo et al. [25] have studied crystallization behavior and magnetic properties of the (Co,Pt)-B-Si system as a function of Pt content. However, no $L1_0$ phase has been obtained due to low Pt concentration in that alloy and amorphous as-cast state was obtained due to the presence of two glass-forming elements (B and Si) with an abundance of 22 at. %.

Additional elements have been introduced in the alloy stoichiometry of FePt-based systems [8,9], to diminish the temperature of the phase transformation and to provide a fine tuning of the as-obtained microstructure. The subsequent purpose is to enhance both the magnetic and structural features. While Nb, Zr, Ag or Mo may act for inhibiting the grain growth, glass-forming elements such as B, Si, and P act to improve the homogeneity of the alloy. It has been shown that Nb addition [9] to FePt enables the enhancement of magnetic properties. Boron added to the stoichiometry [10,11] also ensures improvements of the microstructure. In the case of thin films of composition FePtAg [13] Ag has been beneficial for lowering the temperature of the phase transformation. We have previously shown [18] that Fe-Pt-Ag-B melt-spun alloy shows direct formation of the $L1_0$ phase from the as-cast state without subsequent annealing. It is clear though that the different magnetic features in $L1_0$-based nanocomposite magnets are strongly influenced by their multiphase nanostructures features.

The aim of the present work was to investigate the influence of Co substitution for Fe and the addition of Ag on the formation of nanocomposite structures and on hard magnetic properties of CoPtAgB alloys prepared by rapid solidification from the melt or melt-spinning.

2. Experimental Section

The CoPtAgB alloy has been prepared by melt-spinning under Ar protective atmosphere. The ribbons were synthesized starting with elemental powders of high purity (99.9 wt. %). They were melted together in an induction furnace with controlled melting temperature. Precautions were taken to prevent element segregation and improve the homogeneity of the alloy. With this aim, the primary

molten alloy has been solidified and re-melted 3 times more. A total amount of 5 g has been used for each sample. The rapid solidification of the melt was performed on a Bühler Melt Spinner SC from Edmund Bühler GmbH, Bodelshausen, Germany. The obtained melt was then purged onto the surface of a Cu wheel. The wheel has 40 cm in diameter and rotates during the synthesis at 2000 r/min. The obtained ribbons were about 30 μm thick, 2–3 mm wide and several decimeters long.

Differential scanning calorimetry (DSC) measurement was performed for the rapidly quenched alloys in the range of 300–950 K with a heating rate of 10 K/min. The as-cast samples were annealed at 400 °C (673 K), 473 °C (746 K) and 670 °C (943 K) for 1 h in vacuum. The crystallization processes were monitored using the differential scanning calorimetry (DSC). DSC thermo-analysis has been performed with a Setaram DSC 111 system, from SETARAM Instrumentation, Calure, France, with a range of heating rates between 5 and 50 K/min in temperatures up to 900 K in argon atmosphere.

We have checked by energy dispersion X-ray spectroscopy (EDX) the true chemical composition of all the as-cast samples, to observe the stoichiometry of the alloy and we found no noticeable difference between the nominal composition and the measured one.

Morphology and local atomic structure have been studied using scanning electron microscopy (SEM), high-resolution electron microscopy (HREM) and selected area electron diffraction (SAED). These studies have been carried out using a JEOL JEM ARM 200F electron microscope, from JEOL Ltd., Tokyo, Japan, operated at 200 kV. The specimens for microscopy have been prepared in plan-view orientation by ion milling at 7° angle of incidence and 4 kV accelerating voltage with a Gatan PIPS installation.

The analyses of the crystal structure and the phase composition were carried out using XRD with Cu Kα radiation. The magnetic properties were measured using a with a Superconducting Quantum Interference Device (SQUID), from Quantum Design Europe GmbH, Darmstadt, Germany and the hysteresis loops were performed at room temperature up to 5 T applied field, parallel to the sample plane.

3. Results and Discussion

The phase evolution with temperature plays an important role in establishing the optimal properties of the nanocomposite magnets of $L1_0$-type, since the $L1_0$ phase of interest is stabilized during high-temperature annealing. Therefore, to correctly identify the temperature of the disorder-order phase transformation, thermal analysis either by means of the Differential Scanning Calorimetry (DSC) or Differential Thermal Analysis (DTA) is required. We have performed DSC measurements in a temperature range from 300 K to 900 K with a heating rate of 10 K/min. on the as-cast CoPtAgB alloy. The obtained DSC curve is presented in Figure 1.

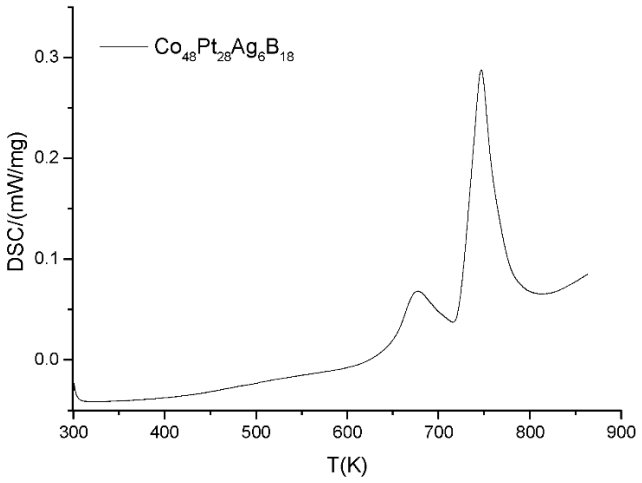

Figure 1. DSC curve for as-cast $Co_{48}Pt_{28}Ag_6B_{18}$ alloy at 10 K/min.

For the sample $Co_{48}Pt_{28}Ag_6B_{18}$ one can observe two separated exothermic peaks well defined at 670 K and 746 K. These peaks represent the thermal signature of the energy exchanged during structural changes of the microstructure of the alloy such as disorder-order transition $L1_0$–A1 and crystallization processes. Using the data obtained through DSC, we have performed isothermal annealing at various temperatures. Parts of CoPtAgB as-cast ribbons have been annealed at different temperatures (400 °C or 673 K, 473 °C or 746 K and 670 °C or 943 K for 1 h each). These values were chosen taking into account the peaks observed in DSC curves. The duration of the annealing has been set for 1 h as a compromise between the need of achieving proper complete phase transformation (as we have seen in other cases that shorter annealing treatments did not lead to complete disorder-order transformation) and the need to restrict as much as possible the grain growth (occurring for longer annealing treatments, e.g., several hours) in order to preserve a refined microstructure with magnetic regions/grains in the nanometer range.

The morphology of the ribbons as observed by Scanning Electron Microscopy (SEM) is presented in Figure 2. SEM images were obtained onto the wheel side of the ribbon surface using a field emission SEM (FE-SEM) with a resolution of 2 nm, under a 30 kV acceleration voltage. It has been documented [26] that there are significant morphological differences between the free side (solidified in Ar) and the wheel side (solidified in contact with the Cu wheel); however, these differences become important for Fe-based melt-spun ribbons in the case of particular effects such as the magneto-impedance observed in soft magnetic ribbons [27].

Both as-cast and annealed samples of $Co_{48}Pt_{28}Ag_6B_{18}$ present a quasi-homogeneous surface with preferred direction of polymorphic growth as indicated by horizontal longitudinal terraces seen in the images. Please note that the surface morphology depends on the initial stoichiometry of the ribbons and on the annealing conditions.

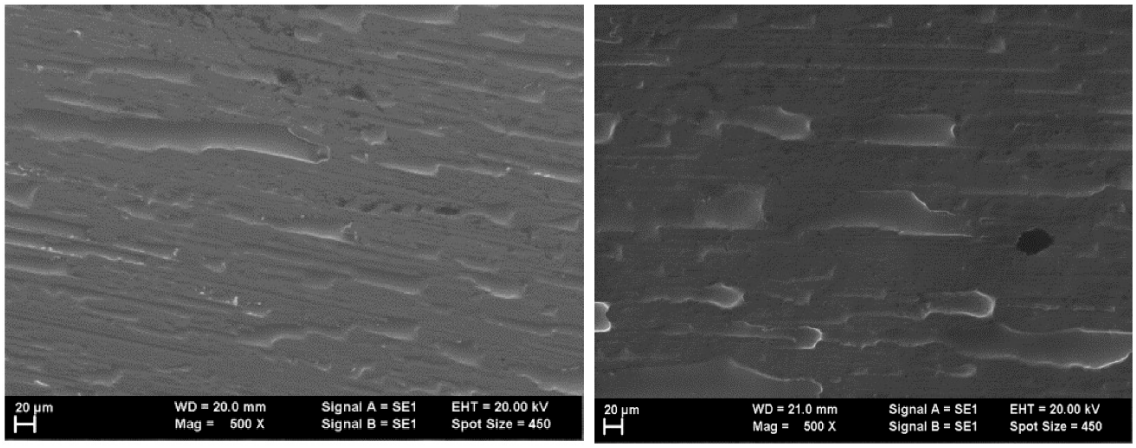

(**a**) (**b**)

Figure 2. (**a**) SEM image of the $Co_{48}Pt_{28}Ag_6B_{18}$ as cast sample; (**b**) SEM image of the $Co_{48}Pt_{28}Ag_6B_{18}$ sample, annealed at 670 °C for 1 h.

The X-ray diffraction analysis was performed using a Bruker D8 Advance diffractometer, from Bruker Nederland BV, Leidendorp, The Netherlands, with Cu Kα radiation (λ = 0.15402 nm) in a Θ–2Θ geometry. The angular interval investigated was between 20 and 100 degrees in 2Θ). All spectra taken have been fitted using a full-profile, Rietveld-type algorithm MAUD (Materials Analysis Using Diffraction) software [28–30] version 2.75, developed by Luca Lutterotti, University of Trento, Italy.

Figure 3 shows the XRD patterns of as-cast and annealed $Co_{48}Pt_{28}Ag_6B_{18}$ samples. For the as-cast and the 400 °C annealed samples, the diffractograms show rather similar features, with broad peaks of low intensity, which belongs to the CoPt face-centered cubic (fcc) phase, space group: *Fm3m*. The situation changes for the samples annealed at higher temperatures. Starting with 473°C annealing,

one can observe additional Bragg peaks, for instance the superlattice peaks (001) and (110) belonging to the $L1_0$ tetragonal CoPt phase, space group: *P4/mmm*, accompanied by a structural refinement and grain growth illustrated by the narrowing of the peak's linewidth and by the evident splitting of some of the peaks belonging to the cubic phase, observed in the previous patterns. More precisely, the (200) peak of the cubic phase splits into the (200) and (002) peaks of the tetragonal phases and the (220) peak of the cubic phase splits into the (220) and (202) peaks of the tetragonal phase. The pattern of the sample annealed at 670 °C shows also the occurrence of the well-formed superlattice peaks (001) and (110) that represents the signature of the $L1_0$ tetragonal CoPt phase. It is also observed that after annealing at 670 °C, the peaks become narrower and the grain size increases.

The average grain size and lattice parameters have been calculated from the fitting of the patterns with the full-profile MAUD algorithm [28–30]. Each Bragg peak has been fitted to a pseudo-Voigt line profile. The Voigt profile, which is represented by a combination of Gaussian and Lorentzian functions whose relative abundance is quantified by the so-called mixing parameter, accounts well for the broadening of the diffraction line by two mechanisms. The first mechanism is related to strain and gives rise to a Gaussian profile, while the second one is related to the size of the grains and would produce a Lorentzian profile.

We have calculated the average grain size, which is here understood as being the average crystallographically coherent domain size, by utilizing the lattice parameters, linewidths and mixing parameters obtained for each Bragg reflection. The method is based on the integral breadth algorithm.

The integral breadth β is defined as the peak area divided by the maximum height of the peak. The integral-breadth method summarized in [31], calculates the root-mean-square (RMS) strain and both surface- and volume-weighted domain sizes according to the "double-Voigt" method [32,33], which is equivalent to the Warren-Averbach approach [34].

In melt-spun ribbons, accounting for different diffusion mechanisms as well as due to the heat loss gradient during rapid quenching, strain is expected to be induced during casting of the ribbons. Consequently, the lattice strain between the atomic planes should be significant. In this respect, RMS strain is defined as the amount (change in size or volume) by which a crystal lattice deforms under stress or force and is given as a ratio of the deformation to the initial size of the lattice. It is only a qualitative indication about the strain induced in the ribbons, though. Detailed, quantitative strain analysis using pole figures and stress tensor measurements as thoroughly done by Kurlyandskaya et al. in [35], though very useful for estimation of magnetoelastic properties, is however outside the scope of our paper.

The average volume-weighted grain size, lattice parameters and RMS strain, calculated from the fitting of the patterns with the full-profile MAUD algorithm, followed using integral breadth method, are presented in Table 1. It is seen that the average grain size increases with the annealing temperatures, ranging from around 20 nm for the as-cast state to 190 nm for the sample annealed at 670 °C, due to the structural refinement imposed by the further crystallization and the disorder-order transition with formation of $L1_0$ tetragonal CoPt from the precursor fcc CoPt phase occurring in the as-cast state.

Table 1. Lattice parameters, average grain sizes obtained from full-profile MAUD analysis.

$Co_{48}Pt_{28}Ag_6B_{18}$	Structure	Lattice Parameters (Å)	Average Grain Size (nm)	RMS Strain (%)
As cast	Fcc CoPt-cubic	$a = 3.729 \pm 0.006$	$D = 20 \pm 3$	0.78 ± 0.08
400 °C	Fcc CoPt-cubic	$a = 3.714 \pm 0.003$	$D = 25 \pm 4$	0.33 ± 0.05
473 °C	$L1_0$ CoPt	$a = 2.650 \pm 0.007$ $c = 3.679 \pm 0.011$	$D = 47 \pm 3$	0.25 ± 0.03
670 °C	$L1_0$ CoPt	$a = 2.674 \pm 0.004$ $c = 3.644 \pm 0.008$	$D = 189 \pm 8$	0.16 ± 0.03

We have also observed an evident RMS strain evolution with the annealing temperature. In the as-cast state, the lattice RMS strain is large (around 0.78%), as expected due to the preparation

conditions and different quenching rates on the two sides (wheel and free) of the ribbons. This strain however diminishes strongly (to around 0.33%) after annealing at 400 °C and this reduces even more for higher annealing temperatures (down to 0.16% after annealing at 670 °C).

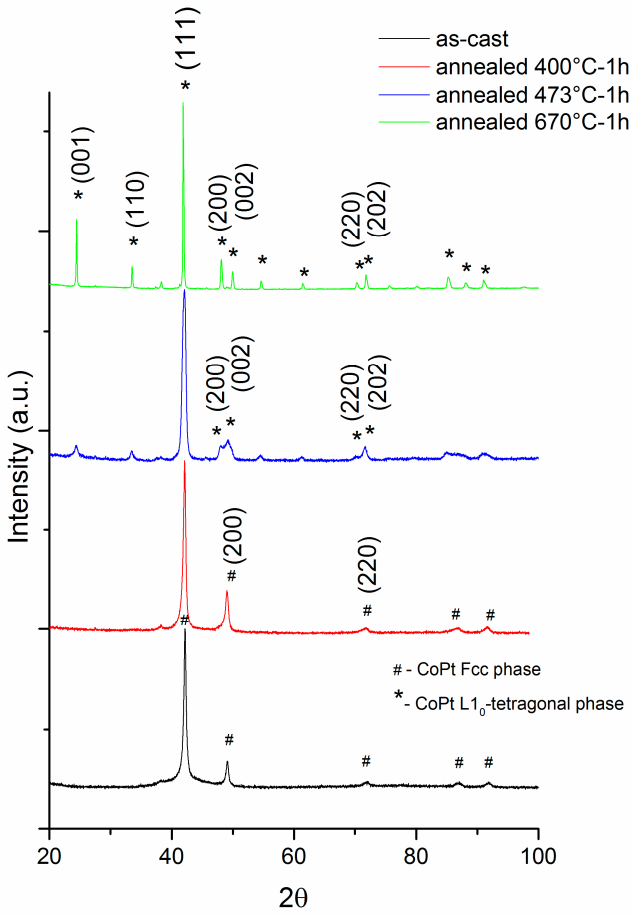

Figure 3. XRD patterns of all investigated samples, as-cast and annealed. The observed phases and reticular planes corresponding to main Bragg peaks are shown on the graph.

Moreover, it is possible from XRD measurements to determine the texture coefficient which can be calculated using the following formula [36,37]:

$$T_{hkl} = n \cdot \left(I_{hkl} / I^0_{hkl} \right) \cdot \sum_n I_{hkl} / I^0_{hkl} \quad (1)$$

T_{hkl} being the texture coefficient of the corresponding Bragg reflection, I_{hkl} its integral intensity as determined by the full-profile fitting of XRD patterns, $I^0{}_{hkl}$ corresponds to the bulk $L1_0$ CoPt Bragg peak intensity (from the ICDD file) and n is the number of Bragg peaks observed.

The texture results for the $L1_0$ CoPt superlattice peaks (001), (110) and (200) are presented in Table 2. One may notice that for the sample annealed at lower temperature, the texture coefficient for all the 3 $L1_0$ superlattice peaks are less than 0.5, indicating that the $L1_0$ CoPt is less ordered. The samples annealed at 670 °C have well-formed and quite intense $L1_0$ superlattice peaks with texture coefficients close to 1. Highest texture coefficient is observed for the (100) Bragg line therefore it may be inferred that there is a slight preferential ordering of the $L1_0$ superlattice in the (100) direction. Other studies on soft magnetic alloy texture have been done by checking the transformation of deformation texture into recrystallization texture during cooling of the alloys [38].

Table 2. The texture coefficients calculated for $L1_0$ superlattice peaks for samples annealed at 473 °C and 670 °C.

$Co_{48}Pt_{28}Ag_6B_{18}$	Texture Coefficient		
	(100)	(110)	(200)
473 °C	0.42	0.38	0.44
670 °C	1.13	0.89	1.01

The findings obtained by XRD have also been confirmed by direct imaging of the microstructure of the as-cast and annealed at 670°C samples, by means of high-resolution transmission electron microscopy (HREM) imaging and selected area electron diffraction (SAED) of the areas imaged in HREM. A representative image of the as-cast $Co_{48}Pt_{28}Ag_6B_{18}$ sample presented in Figure 4 confirms the fact that the disordered fcc phase (*Fm3m*) is predominant in this sample. Large grain areas (between 10 nm and 25 nm lateral size) with planes separated by reticular distances that reveal the occurrence of (200) and (222) reflections are shown in Figure 1.

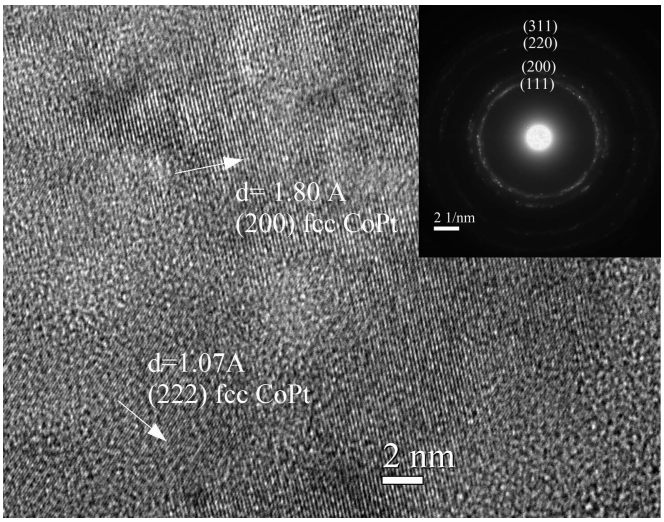

Figure 4. An area of the as-cast $Co_{48}Pt_{28}Ag_6B_{18}$ sample showing (200) and (222) planes of fcc CoPt phase; Inset: the SAED pattern.

In the associated SAED pattern (Figure 4, inset), the most intense (111) and the (200), (220) and (311) diffraction rings of fcc CoPt phase can be identified. From the observed diffraction rings a value of lattice constant of $a = 3.72 \pm 0.005$ Å was calculated, in good agreement with the value $a = 3.729$ Å determined from XRD for this sample. In some diffraction patterns, an additional diffraction ring, observable at $d = 2.12$ Å, could be attributed to the (111) plane of ordered rhombohedral phase $L1_1$, reported by previous authors [1,21] as being a metastable phase that precedes the formation of the tetragonal $L1_0$ phase during the disorder-order phase transformation, and having $a = 5.34$ Å and $\alpha = 61.5°$ as lattice parameters.

The HREM image of the $Co_{48}Pt_{28}Ag_6B_{18}$ sample annealed at 670 °C is shown in Figure 5. In the image, areas of $L1_0$ phase (between 5–20 nm lateral size) are shown and the (101) and (110) lattice planes are clearly visualized, in good agreement with XRD patterns obtained for the sample annealed at 670 °C.

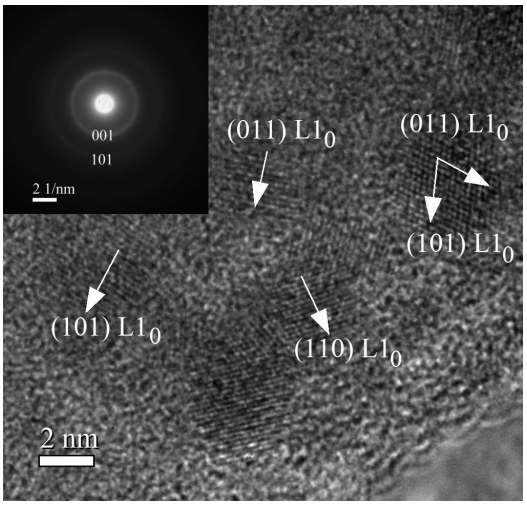

Figure 5. An area of the $Co_{48}Pt_{28}Ag_6B_{18}$ sample annealed at 670 °C showing $L1_0$ phase zones containing lattice planes of (101) and (110); Inset: the associated SAED pattern.

SAED patterns have a polycrystalline nature as revealed by the most intense ring (101) which could be continuous (as in the inset of Figure 5) in the case of large ordered areas or consisting of many spots in the case of smaller ordered regions. In the first case one can also observe the (001) ring typical for the $L1_0$ superstructure whereas only a weak (110) ring is apparent in the second case.

Figure 6 shows a SAED pattern of the same $Co_{48}Pt_{28}Ag_6B_{18}$ sample annealed at 670 °C which confirms that there are large ordered regions of $L1_0$ phase, as confirmed in some cases in SAED patterns which show, besides the (002) spot, the (001) and the rarely observed and indexed (003) superlattice peak, characteristic to the high level of ordering of the $L1_0$ phase, whereas in XRD patterns only (001) and (002) superlattice peaks are observed. It is of interest to note that the higher the order of the superlattice peaks observed, i.e., higher l in the (00l) notation of the observed peaks indexation, the higher the degree of ordering of the $L1_0$ phase.

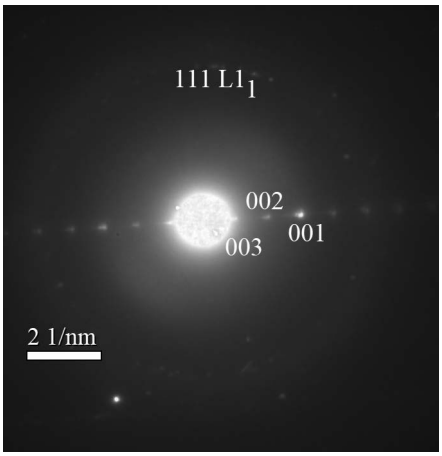

Figure 6. A SAED pattern showing, besides the (002) spot, the superlattice peaks (001) and (003) characteristic to the highly ordered fct $L1_0$ phase.

The hysteresis loops of the samples $Co_{48}Pt_{28}Ag_6B_{18}$ as-cast and annealed at 670 °C (Figure 7) have been recorded using SQUID magnetometry with the applied field parallel to the ribbons plane. The magnetic field was applied up to 50,000 Oe and measurements were taken at 300 K (or 27 °C). For the as-cast sample, it is observed that the hysteresis loop shows strong approach to the saturation at relatively low applied magnetic field (few hundreds of Oe). A large value of maximum magnetization

(82 emu/g for a maximum applied field of 50,000 Oe) is then reached. The loop also exhibits very low coercivity. The exact value of the coercive field is estimated between 270 and 370 Oe. The lack of more experimental points in that region impedes furnishing of a more accurate value for the coercivity; however, the magnetic behavior is consistent with the presence of the disordered fcc A1 CoPt phase in the sample. Also, a detailed theoretical approach to saturation of the magnetization requires modeling, similar to the one presented in [39].

The magnetic behavior of the annealed sample is quite different. The approach to saturation of the magnetization is slower, eventually reaching 80 emu/g only at around 32,000 Oe applied field. More importantly, the hysteresis loop shows up to 10 times increase of the coercivity (about 4340 Oe). This dramatic increase of the coercivity corroborates the structural results, as such large values are typical for hard magnetic materials such as the ones exhibiting pure $L1_0$ phase (either CoPt or FePt). Indeed, such large values of coercivity at 300 K observed in the annealed sample confirm the results obtained in HREM and XRD where the highly ordered $L1_0$ CoPt phase is documented, inclusively by the presence of the rarely observed (003) superlattice ring in SAED patterns.

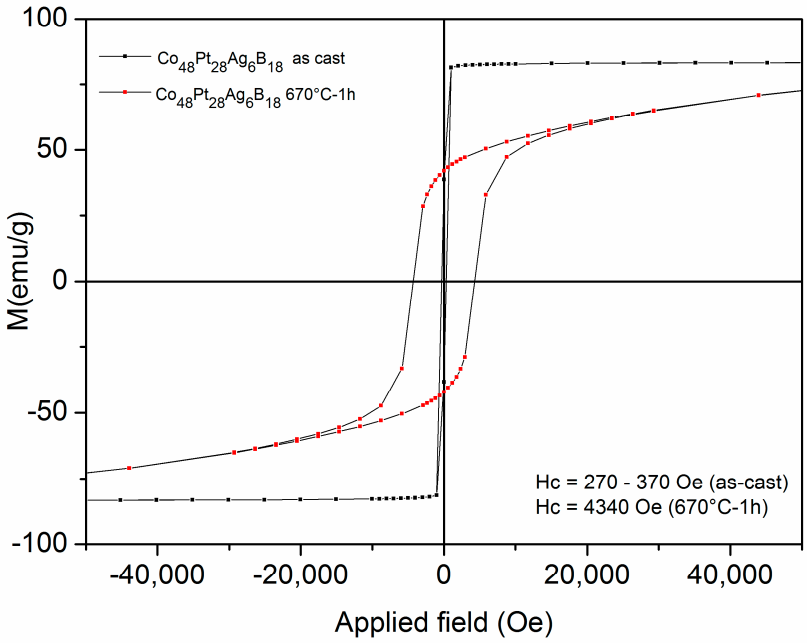

Figure 7. The hysteresis loops of the samples $Co_{48}Pt_{28}Ag_6B_{18}$ as-cast and annealed at 670 °C.

In fact, the material can be regarded as a composite that contains magnetic particles/regions of a nanometric scale embedded in a structurally and magnetically disordered residual matrix. The magnetic behavior is however consistent with results previously published in [40] and the magnetic behavior of $L1_0$ CoPt nanoparticles as described in [41]. In both papers, the evolution with annealing parameters (time, temperature) is studied and the results show that the magnetic behavior is typical for multiphase materials, with coercivity lightly reduced, as compared to bulk $L1_0$ CoPt, due to the interphase interactions between the hard magnetic $L1_0$ CoPt grains and the disordered magnetic intergrain regions (or embedding matrix).

4. Conclusions

In search for new nanocomposite magnets based on $L1_0$ phase, a detailed thermal, structural, and magnetic study of the $Co_{48}Pt_{28}Ag_6B_{18}$ alloy has been undertaken. Thermal analysis revealed the exothermic peaks attributable to the $L1_0$ ordering temperature and crystallization processes. The evolution of the phase structure with temperature has been investigated. In that purpose, several annealings at 400 °C, 473 °C and 670 °C for 1 h each have been performed and the structure of the

resulting samples have been investigated by XRD and HREM. It has been revealed that for lower annealing temperatures (400 °C) the microstructure consists of crystallized regions of soft magnetic fcc CoPt phase, but, starting with 473 °C annealings, the hard magnetic $L1_0$ phase becomes predominant. It is shown that at 670 °C the $L1_0$ phase achieves a high degree of ordering as proven by the occurrence of the rarely observed (003) superlattice peak. Furthermore, the hysteresis loop of the annealed sample shows up to 10 times increase of the coercivity (about 4340 Oe) compared to the as-cast one. These findings are promising in view of use of such materials as a future class of rare-earth free-permanent magnets.

Author Contributions: Conceptualization, A.D.C. and O.C.; Methodology, I.M.; Software, A.D.C.; Formal Analysis, F.V.; Investigation, C.B. and M.E.; Writing-Original Draft Preparation, A.D.C.; Writing-Review & Editing, O.C.

Funding: This research was funded by Ministerul Educației și Cercetării Științifice grant number PN-III-P4-ID-PCE-2016-0833 and through POC Project P_37_697 (28/01.09.2016) "Boron- and rare-earths-based advanced functional materials" of the Romanian National Authority for Scientific Research and Innovation.

Conflicts of Interest: The authors declare no conflict of interest. The funding sponsors had no role in the design of the study; in the collection, analyses, or interpretation of data; in the writing of the manuscript, and in the decision to publish the results.

References

1. Sun, A.C.; Yuan, F.T.; Hsu, J.H.; Lee, H.Y. Evolution of structure and magnetic properties of sputter-deposited CoPt thin films on MgO (1 1 1) substrates: Formation of the $L1_1$ phase. *Scr. Mater.* **2009**, *61*, 713–716. [CrossRef]
2. Huang, C.F.; Chen, Y.S.; Sun, A.C.; Huang, C.F. Growth of $L1_1$ structured CoPt thin films by alternate sputtering method on glass substrate. *Surf. Coat. Technol.* **2016**, *303*, 131–135. [CrossRef]
3. Chen, Y.S.; Sun, A.C.; Lee, H.Y.; Lu, H.C.; Wang, S.F.; Sharma, P. Enhanced coercivity of HCP Co–Pt alloy thin films on a glass substrate at room temperature for patterned media. *J. Magn. Magn. Mater.* **2015**, *391*, 12–16. [CrossRef]
4. Shen, C.L.; Kuo, P.C.; Li, Y.S.; Lin, G.P.; Ou, S.L.; Huang, K.T.; Chen, S.C. Thickness dependence of microstructures and magnetic properties for CoPt/Ag nanocomposite thin films. *Thin Solid Films* **2010**, *518*, 7356–7574. [CrossRef]
5. Kushibiki, R.; Tham, K.K.; Hinata, S.; Saito, S. High Ku and small grain size $Co_{80}Pt_{20}$ granular media with double oxide grain boundary materials consisting of B_2O_3. *AIP Adv.* **2017**, *7*, 05651. [CrossRef]
6. Xiao, Q.F.; Brűck, E.; Zhang, Z.D.; de Boer, F.R.; Buschow, K.H.J. Remanence enhancement in nanocrystalline CoPt bulk magnets. *J. Alloys Compd.* **2002**, *336*, 41–45. [CrossRef]
7. Crisan, A.D.; Nicula, R.; Crisan, O.; Burkel, E. Thermally and pressure activated phase evolution in Fe-Pt-Nb-B melt spun ribbons. *Mater. Sci. Eng. C* **2007**, *27*, 1280–1282. [CrossRef]
8. Crisan, O.; Crisan, A.D.; Randrianantoandro, N.; Nicula, R.; Burkel, E. Crystallization processes and phase evolution in amorphous Fe-Pt-Nb-B alloys. *J. Alloys Compd.* **2007**, *440*, L3–L7. [CrossRef]
9. Bruck, E.; Xiao, Q.F.; Thang, P.D.; Toonen, M.J.; de Boer, F.R.; Buschow, K.H.J. Influence of phase transformation on the permanent-magnetic properties of Fe-Pt based alloys. *J. Phys. B* **2001**, *300*, 215–229. [CrossRef]
10. Makino, A.; Bitoh, T. High coercivity of melt-spun $(Fe_{0.55}Pt_{0.45})_{78}Zr_{2-4}B_{18-20}$ nanocrystalline alloys with $L1_0$ structure. *J. Appl. Phys.* **2004**, *95*, 7498–7500. [CrossRef]
11. Makino, A.; Bitoh, T.; Inoue, A.; Hirotu, Y. Magnetic properties and structure of Fe–Pt–M–B (M = Zr, Nb and Ti) alloys produced by quenching technique. *J. Alloys Compd.* **2007**, *434*, 614–617. [CrossRef]
12. Crisan, A.D.; Crisan, O.; Randrianantoandro, N.; Valeanu, M.; Morariu, M.; Burkel, E. Crystallization processes in Fe-Pt-Nb-B melt spun ribbons. *Mater. Sci. Eng. C* **2007**, *27*, 1283–1285. [CrossRef]
13. Randrianantoandro, N.; Crisan, A.D.; Crisan, O.; Marcin, J.; Kovac, J.; Hanko, J.; Greneche, J.M.; Svec, P.; Chrobak, A.; Skorvanek, I. The influence of microstructure on magnetic properties of nanocrystalline Fe–Pt–Nb–B permanent magnet ribbons. *J. Appl. Phys.* **2010**, *108*, 093910. [CrossRef]
14. Wang, S.; Kang, S.S.; Nikles, D.E.; Harrell, J.W.; Wu, X.W. Magnetic properties of self-organized $L1_0$ FePtAg nanoparticle arrays. *J. Magn. Magn. Mater.* **2003**, *266*, 49–56. [CrossRef]

15. Crisan, O.; Angelakeris, M.; Flevaris, N.K. Magnetism and anisotropy in core-shell nanoparticles. *J. Optoelectron. Adv. Mater.* **2003**, *5*, 959–962.
16. Gonzalez, J.A.; Andres, J.P.; de Toro, J.A.; Muñiz, P.; Muñoz, T.; Crisan, O.; Binns, C.; Riveiro, J.M. Co–CoO nanoparticles prepared by reactive gas-phase aggregation. *Nanopart. Res.* **2009**, *11*, 2105–2111. [CrossRef]
17. Reddy, V.R.; Crisan, O.; Gupta, A.; Banerjee, A.; Kuncser, V. Tuning exchange spring effects in FePt/Fe(Co) magnetic bilayers. *Thin Solid Films* **2012**, *520*, 2184–2189. [CrossRef]
18. Crisan, A.D.; Crisan, O. Direct formation of $L1_0$ FePt in as-cast FePt-based magnetic nanocomposite ribbons without post-synthesis annealing. *J. Phys. D Appl. Phys.* **2011**, *44*, 365002. [CrossRef]
19. Crisan, A.D. Compositional studies and thermal analysis in amorphous and nanocrystalline FePtNbB melt spun ribbons. *J. Optoelectron. Adv. Mater.* **2010**, *12*, 250–256.
20. Rosenberg, M.; Kuncser, V.; Crisan, O.; Filoti, G. A Mössbauer Spectroscopy and Magnetic Study of FeRh. *J. Magn. Magn. Mater.* **1998**, *177*, 135–136. [CrossRef]
21. Iwata, S.; Yamashita, S.; Tsunashima, S. Perpendicular magnetic anisotropy and magneto-optical Kerr spectra of MBE-grown PtCo alloy films. *IEEE Trans. Magn.* **1997**, *33*, 3670–3672. [CrossRef]
22. Chang, C.W.; Chang, H.W.; Chiu, C.H.; Hsieh, C.C.; Fang, Y.K.; Chang, W.C. Magnetic property improvement of Pt-lean FePt/Fe–B-type nanocomposites by Co substitution. *J. Appl. Phys.* **2008**, *103*, 07E133. [CrossRef]
23. Makino, A.; Bitoh, T.; Nakagawa, M. Direct synthesis of $L1_0$-(Fe, Co)Pt nanocrystallites from (Fe, Co)–Pt–Zr–B liquid phase by melt-spinning. *J. Non-Cryst. Solids* **2007**, *353*, 3655–3660. [CrossRef]
24. Inoue, A.; Zhang, W. Nanocrystalline Fe-Pt-B base hard magnets with high coercive force obtained from amorphous precursor. *J. Appl. Phys.* **2005**, *97*, 10H308. [CrossRef]
25. Yoo, C.S.; Lim, S.K.; Yoon, C.S.; Kim, C.K. Crystallization of Co_{100-x} $Pt_xB_{10}Si_{12}$ amorphous metallic alloys. *Metall. Mater. Trans. A* **2004**, *35A*, 2057–2061. [CrossRef]
26. Lotfollahi, Z.; García-Arribas, A.; Amirabadizadeh, A.; Orue, I.; Kurlyandskaya, G.V. Comparative study of magnetic and magnetoimpedance properties of CoFeSiB-based amorphous ribbons of the same geometry with Mo or W additions. *J. Alloys Compd.* **2017**, *693*, 767–776. [CrossRef]
27. Chaturvedi, A.; Dhakal, T.; Witanachchi, S.; Le, A.-T.; Phan, M.-H.; Srikanth, H. Correlation between magnetic softness, sample surface and magnetoimpedance in $Co_{69}Fe_{4.5}X_{1.5}Si_{10}B_{15}$ (X = Ni, Al, Cr) amorphous ribbons. *Phys. B Condens. Matter* **2010**, *405*, 2836–2839. [CrossRef]
28. Ferrari, M.; Lutterotti, L. Method for the simultaneous determination of anisotropic residual stresses and texture by x-ray diffraction. *J. Appl. Phys.* **1994**, *76*, 7246–7255. [CrossRef]
29. Wenk, H.-R.; Matthies, S.; Lutterotti, L. Texture analysis from diffraction spectra. *Mater. Sci. Forum* **1994**, *157–162*, 473–480. [CrossRef]
30. Matthies, S.; Lutterotti, L.; Wenk, H.-R. Advances in Texture Analysis from Diffraction Spectra. *J. Appl. Crystallogr.* **1997**, *30*, 31–42. [CrossRef]
31. Klug, H.P.; Alexander, L.E. *X-ray Diffraction Procedures*, 2nd ed.; John Wiley: New York, NY, USA, 1974.
32. Balzar, D.; Ledbetter, H. Voigt-function modeling in Fourier analysis of size- and strain-broadened X-ray diffraction peaks. *J. Appl. Crystallogr.* **1993**, *26*, 97–103. [CrossRef]
33. Balzar, D. X-Ray Diffraction Line Broadening: Modeling and Applications to High-Tc Superconductors. *J. Res. Natl. Inst. Stand. Technol.* **1993**, *98*, 321–353. [CrossRef] [PubMed]
34. Warren, B.E. *X-ray Diffraction*; Addison Wesley: Reading, MA, USA, 1969.
35. Kurlyandskaya, G.V.; Lukshina, V.A.; Larrañaga, A.; Orue, I.; Zaharova, A.A.; Shishkin, D.A. Induced magnetic anisotropy features in FeCrSiBNbCu nanocrystalline alloy: Role of stress distribution proven by direct X-ray measurements. *J. Alloys Compd.* **2013**, *566*, 31–36. [CrossRef]
36. Li, J.J.; Hu, L.F.; Li, F.Z.; Li, M.S.; Zhou, Y.C. Variation of microstructure and composition of the Cr2AlC coating prepared by sputtering at 370 and 500 °C. *Surf. Coat. Technol.* **2010**, *204*, 3838–3845. [CrossRef]
37. Lee, D.N. Textures and structures of vapor deposits. *J. Mater. Sci.* **1999**, *34*, 2575–2582. [CrossRef]
38. Aryshenskii, E.V.; Aryshenskii, V.Y.; Grechnikova, A.F.; Beglov, E.D. Evolution of Texture and Microstructure in the Production of Sheets and Ribbons from Aluminum Alloy 5182 in Modern Rolling Facilities. *Met. Sci. Heat Treat.* **2014**, *56*, 347–352. [CrossRef]
39. Komogortsev, S.V.; Iskhakov, R.S. Law of approach to magnetic saturation in nanocrystalline and amorphous ferromagnets with improved transition behavior between power-law regimes. *J. Magn. Magn. Mater.* **2017**, *440*, 213–216. [CrossRef]

40. Luong, N.H.; Hai, N.H.; Phu, N.D.; MacLaren, D.A. Co-Pt nanoparticles encapsulated in carbon cages prepared by sonoelectrodeposition. *Nanotechnology* **2011**, *22*, 285603. [CrossRef] [PubMed]
41. Komogortsev, S.V.; Chizhik, N.A.; Filatov, E.Y.; Korenev, S.V.; Shubin, Y.V.; Velikanov, D.A.; Iskhakov, R.S.; Yurkin, G.Y. Magnetic Properties and $L1_0$ Phase Formation in CoPt Nanoparticles. *Solid State Phenom.* **2012**, *190*, 159–162. [CrossRef]